# Chemical Science

## Accepted Manuscript

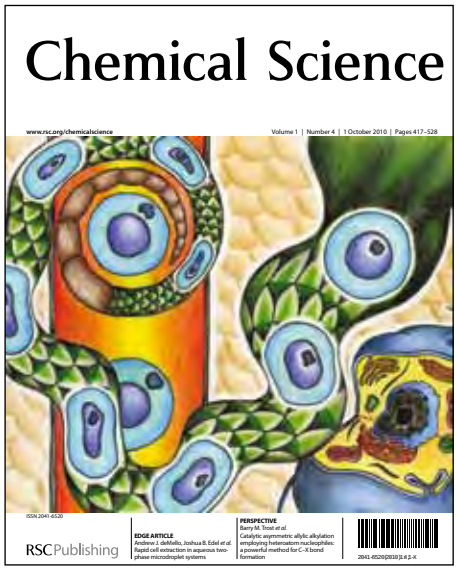


This is an *Accepted Manuscript*, which has been through the RSC Publishing peer review process and has been accepted for publication.

*Accepted Manuscripts* are published online shortly after acceptance, which is prior to technical editing, formatting and proof reading. This free service from RSC Publishing allows authors to make their results available to the community, in citable form, before publication of the edited article. This *Accepted Manuscript* will be replaced by the edited and formatted *Advance Article* as soon as this is available.

To cite this manuscript please use its permanent Digital Object Identifier (DOI®), which is identical for all formats of publication.

More information about *Accepted Manuscripts* can be found in the **Information for Authors**.

Please note that technical editing may introduce minor changes to the text and/or graphics contained in the manuscript submitted by the author(s) which may alter content, and that the standard **Terms & Conditions** and the **ethical guidelines** that apply to the journal are still applicable. In no event shall the RSC be held responsible for any errors or omissions in these *Accepted Manuscript* manuscripts or any consequences arising from the use of any information contained in them.

Chemical Science

RSCPublishing

EDGE ARTICLE

# Atomic properties and chemical bonding in the pyrite and marcasite polymorphs of $FeS_2$: A combined experimental and theoretical electron density study

Cite this: DOI: 10.1039/x0xx00000x

Received 00th January 2012,
Accepted 00th January 2012

DOI: 10.1039/x0xx00000x

www.rsc.org/chemicalscience

Mette S. Schmøkel,[a] Lasse Bjerg,[a] Simone Cenedese,[b, d] Mads R. V. Jørgensen,[a] Yu-Sheng Chen,[c] Jacob Overgaard,*[a] Bo B. Iversen*[a]

The electron density distributions in both polymorphs of the promising photovoltaic material iron disulphide have been determined by multipole modelling against state-of-the-art synchrotron X-ray diffraction data collected at 10 K using minute single crystals with dimensions less than 10 μm. Charge density analysis of $FeS_2$ pyrite and marcasite offers a unique opportunity to relate local atomic properties, such as 2-center chemical bonding, atomic charges and d-orbital populations, to polymorphism in extended crystal structures. In combination with results from periodic calculations on the compounds in the experimental geometries using WIEN2k, the study provides unambiguous answers to a number of unsolved issues regarding the nature of the bonding in $FeS_2$. The Fe-S bonds exhibit all the virtues of polar covalent bonds, with only minor charge accumulation but significantly negative energy densities at the bond critical points. Compared to a non-interacting model, the density is found to be concentrated along the Fe-S interaction line in support of a partial covalent bonding description. The homopolar covalent S-S interaction is seemingly stronger in pyrite than in marcasite, determined not only from the shorter distance but also from all topological indicators. The study also clarifies that the atomic charges are significantly smaller than the estimation based on crystal-field theory of $Fe^{2+}$, $S^{-1}$. The experimentally derived Fe d-orbital populations are found to deviate from the commonly assumed full $t_{2g}$ set, empty $e_g$ set, and they fit exceptionally well with the theoretical individual atomic orbitals projected density of states showing a higher $d_{xy}$ participation in the valence band in marcasite compared with pyrite. Thus, the differences between the two polymorphic compounds are directly reflected in their valence density distributions and d-orbital populations.

## Introduction

$FeS_2$ has played a role in crystallography from the very birth of the field, and the crystal structure of the pyrite $FeS_2$ polymorph was among the first structures to be solved by Bragg using the X-ray diffraction technique.[1, 2] More recently, iron pyrite has attracted strong attention due to its photovoltaic properties: it combines a suitable band gap of 0.9 eV, an impressive optical absorption coefficient of the order $10^5$ $cm^{-1}$, high abundance and availability with non-toxicity of the constituents, thereby making it a candidate for future solar cell materials.[3-7] Unfortunately, these promising properties have never been exploited in actual applications, and many reasons for this have been mentioned, including the presence of surface states as gap states having a detrimental effect on the band gap, or the presence of epitaxial growth of the other, less stable $FeS_2$ polymorph, marcasite, on the pyrite surfaces.[3] Nevertheless, due to the significant potential that $FeS_2$ holds, applications of the pyrite polymorph in photovoltaic devices is far from abandoned.[8, 9] Consequently, the structure and bonding in both of the two $FeS_2$ polymorphs is a topic of continuing widespread scientific interest. Historically, the original bonding schemes of the $FeS_2$ pyrite, marcasite and other related $MX_2$ structures date back more than 40 years and were based on the crystallographic and structural differences between the compounds.[10-23] More sophisticated approaches were naturally since adopted, including a study of the bonding trends in a range of iron sulphide compounds using topological analysis of theoretical electron densities by Gibbs *et al.*[24, 25] Furthermore, it should also be noted that iron pyrite was the subject of one of the

earliest experimental electron density studies involving a transition-metal element,[26] and quantitative d-orbital splitting of the iron site was derived from multipole refinement against X-ray diffraction data. The present study of $FeS_2$ is one of only a few X-ray electron density studies appearing in the literature on periodic, inorganic, 'heavy'-element compounds, despite their interesting physical and chemical properties.[27] The reason for this may be attributed to the great challenges related to obtaining high-quality data with limited absorption and extinction effects. The low scattering contribution from the valence electrons and their often diffuse character place high demands on the accuracy of the low-order data.[28] We have in recent years developed approaches to overcome these challenges in order to obtain accurate experimental electron densities of inorganic compounds as was recently shown for both $K_2SO_4$[29] and $CoSb_3$.[30, 31] A unique feature of the present study is the use of unprecedented small crystals for an experimental electron density study (< 10 μm). This provides a remarkable reduction in systematic errors from absorption and extinction effects.

In the present paper we take full advantage of our previous experiences and report a combined theoretical and experimental study of the electron density distribution (EDD, $\rho$) in both polymorphs of $FeS_2$, cubic pyrite and orthorhombic marcasite. A topological analysis of the EDD using Bader's Quantum Theory of Atoms in Molecules (QTAIM)[32] allows for a detailed quantitative examination of the chemical bonding in the structure. The study has particular focus on the nature of the 2-center chemical bonds as well as the distribution of d-electrons around Fe. In addition, the QTAIM analysis of the density automatically provides a division of space enabling the calculation of atomic charges and dipoles. These are crucial for a derivation of the cohesive energy of the crystal structures as described by Birkholz.[33] Most importantly, internal comparison of properties between the two polymorphs is of considerable interest. There has been relatively few experimental electron density studies of polymorphic systems[34-43] and this is the first on a dimorphic binary extended solid.

The paper is organized in four parts. In part 1, the crystal structures of both polymorphs are described in detail along with a brief outline of how the understanding of the nature of the bonding has developed over time up to the current view. Part 2 outlines the experimental methods and practices used to reach the electron density models. In part 3, the nature of the Fe-S and S-S bonding is described, while part 4 focuses on the atomic EDD around the Fe-sites and its agreement with band structure calculations and magnetic measurements. Of particular interest is the remarkable agreement between the d-orbital populations derived from multipole fitting of the experimental density and those obtained from the individual atomic orbitals projected density of states (DOS).

## Part 1. Structure and bonding in $FeS_2$

### 1.1 Crystal structures

Pyrite and marcasite are polymorphs of iron sulphide, $FeS_2$. Pyrite crystallizes in the cubic space group, *Pa-3* while marcasite belongs to orthorhombic *Pnnm*. As pointed out by several authors, the marcasite and pyrite structures can both be described in terms of trigonally distorted $FeS_6$ octahedra and tetrahedrally coordinated sulphur atoms (Figure 1).[10, 14, 44] However, some differences can be highlighted. In pyrite the crystal structure is constructed entirely by corner-sharing octahedra, and according to the local symmetry ($S_6/C_{3i}$, -3) of the Fe atom at the (0,0,0) site, all the Fe-S interactions are equivalent. On the other hand, the $FeS_6$ units in marcasite are edge-sharing along the unit cell *c*-axis and corner-sharing in the other directions (Figure 1). Accordingly, the Fe site, also at (0,0,0), has a lower symmetry ($C_{2h}$, 2/*m*) and two different kinds of Fe-S interactions are found: two short 'axial' bonds and four long 'equatorial' bonds. The sulphur atom is coordinated to three iron atoms and one other sulphur in both pyrite and marcasite, however, in pyrite the sulphur at (*x*,*x*,*x*) has $C_3$ symmetry (3-fold rotation axis), whereas the only symmetry associated with the (*x*,*y*,0) sulphur site in marcasite is a mirror plane.

The rather short S-S interaction (Table 1) of the disulphide unit creates an $S_2$ dumbbell (for comparison, the S-S bond distance in $S_8$ is ~2.04 Å[45]), which along with the $FeS_6$ octahedra are the main structural features that characterize these structures. In both structures the $S_2$ dumbbells provide additional contact between the octahedra, however, in marcasite they are stacked along the *c* direction in a ladder-like structure (see Figure 2).[10, 12, 15, 46] Contrary to the Fe-S interactions which are longer in pyrite than in marcasite, the S-S distance in pyrite is shorter than in marcasite. Kjekshus & Nicholson[16] as well as Stevens *et al.*[26] have proposed that a strengthening of the Fe-S interaction will cause a weakening of the S-S bond due to charge depletion or destabilization of the S-S pair. This possibly explains why the longer S-S interaction is found in the marcasite structure with the shorter Fe-S bonds.[16, 26] An excellent description of the differences in the structure of these two polymorphs as well as relations to other similar structures has been given by Hyde & O'Keeffe.[22]

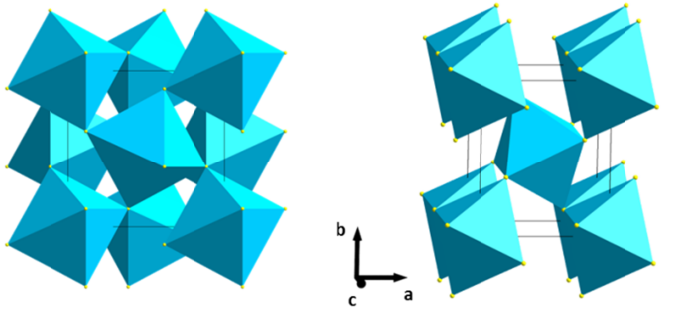


Figure 1. The structure of pyrite (left) and marcasite (right) represented in terms of $FeS_6$ octahedra. S atoms are shown as small yellow spheres. The unit cells are indicated by black lines; the *ab* plane of marcasite is in the plane of the paper.

Table 1. Experimental geometry of the pyrite and marcasite structures.

| | Pyrite | Marcasite |
|---|---|---|
| d(Fe-S) (Å) | 2.26312(1) | 2.23551(7), 2.25299(5) |
| ∠(S-Fe-S) | 85.6477(5)° | 82.464(3)°, 87.984(1)° |
| d(S-S) (Å) | 2.1597(1) | 2.2119(2) |

### 1.2 Historical bonding schemes.

The edge-sharing of the octahedra along the *c*-axis in marcasite causes the Fe-Fe distance to be shorter in this direction ($d_{Fe-Fe}$ ~ 3.38 Å) than along any other direction in the structure and shorter than the Fe-Fe distance in pyrite ($d_{Fe-Fe}$ ~ 3.83 Å). In 1968 it was suggested by Nickel that the small S-Fe-S angle (α in Figure 2) and the 'elongation' of the equatorial Fe-S bonds with respect to the axial ones is caused by Fe-Fe repulsion along the *c* direction between the filled d-orbitals ($d_{xy}$) on nearest-neighbour iron atoms.[12] In order to explain the stability of the marcasite structure in spite of this repulsion, additional 'long-range' interactions between the $S_2$ dumbbells, stacked along the *c*-axis, were suggested.[47] As shown below, no indications of such interactions have been found in the present study.

Nickels arguments were based on the work of Pearson (1965)[47] and Hulliger and Mooser (1965)[10] who were the first to rationalize the structural and physical properties of $FeS_2$ in terms of the iron d-electron distribution. According to crystal field theory,[48] a purely electrostatic octahedral field ($O_h$) will cause the d-levels to split into three lower-energy, non-bonding $t_{2g}$ states, and two higher-energy, anti-bonding $e_g$ states. However, the trigonal distortion of the $FeS_6$ octahedra due to the crystal field causes a further splitting of the $e_g$ and $t_{2g}$ levels for each of the structures as illustrated in Figure 2.[10] In order to explain the semiconducting, diamagnetic properties of the compounds, Hulliger and Mooser proposed an ionic bonding scheme according to which the 4s electrons on Fe are fully transferred to the $S_2$ unit thereby fulfilling the octet rule for sulphur. In order to explain the lack of metallic conduction, they assumed a low-spin $d^6$ configuration on iron in which the electrons would fully occupy the non-bonding $t_{2g}$ states.

In 1970 Brostigen and Kjekshus further developed the idea of Fe-Fe repulsion with their so-called *expansion model*; however, they entirely rejected the notion of additional S-S interactions.[14, 49] Instead they characterized the bonding interactions in $FeS_2$ based on qualitative band structures derived from ligand field theory in terms of molecular orbital (MO) diagrams which was already proposed for iron pyrite in 1968 by Bither *et al.*[50, 51] (see Figure S2 in the Supporting Information). They concluded that the 3d($e_g$), 4s, and 4p states on Fe combine with the valence orbitals on S to form six bonding orbitals (which turn into bands in the crystal structure) associated with each $FeS_6$ octahedron, while the 3d($t_{2g}$) states on iron are assumed to be localized and non-bonding. Additionally, one bonding band is associated with the S-S interaction leading to a total of seven filled bonding and seven empty anti-bonding bands in agreement with the semiconducting properties of both compounds. The authors note that this description could, in principle, be consistent with the ionic $Fe^{2+}S_2^{2-}$ bonding description which was originally proposed by Hulliger and Mooser. However, based on the lack of ionic conductivity and d-level splitting considerations, they end up rejecting the ionic model in favour of a covalent description.[49] Already back in 1934, a covalent bonding description was suggested by Pauling and Huggins involving overlap of $d^2sp^3$ hybrid orbitals on Fe with $sp^3$ hybridized orbitals on S forming six Fe-S and one S-S single bond per formula unit,[52] and this hybridization has later been supported by various electronic structure calculations.[6, 17, 46, 53-57] In spite of this, $FeS_2$ continues to be approximated as composed of largely ionic $Fe^{2+}$ and $S_2^{2-}$ units in several succeeding studies.[3, 4, 58, 59]

In 1972, Goodenough elaborated on the band structure models of Brostigen and Kjekshus in an attempt to explain the origin of the difference between various $MX_2$ structures. In spite of its explanatory and predictive power, the expansion model was rejected based on the argument that any such Fe-Fe interaction would be attractive instead of repulsive. The elongation along the *c* direction was explained in terms of repulsion between M and X resulting from the occupation of the metal (M) $d_{xy}$ orbital setting in when the total d-orbital population exceeds four, as in the case of $FeS_2$. Goodenough further argued that the resulting reduction in stabilization of marcasite structures with more than four d-electrons cause the energy of these compounds to be similar to that of the corresponding pyrite structure.[19] This is in agreement with theoretical and experimental results showing that the stability of $FeS_2$ pyrite and marcasite is similar, with the marcasite structure primarily forming at low temperatures under acidic conditions and the slightly more stable pyrite structure forming preferentially at higher temperatures.[3, 12, 17, 60-64]

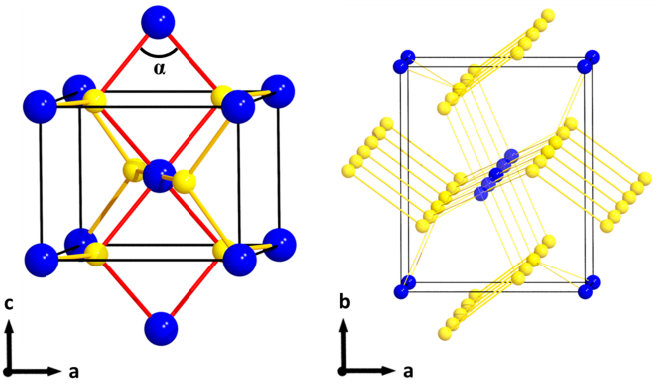

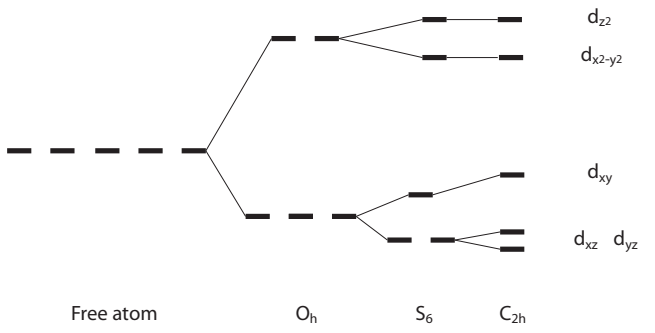


Figure 2. Top: Edge-sharing of octahedra (left) and $S_2$ dumbbells (right) along the *c*-axis in marcasite. The long, equatorial Fe-S interactions are shown in red (α~82°). Bottom: Qualitative crystal field splitting of the Fe 3d levels in pyrite ($S_6$) and marcasite ($C_{2h}$) according to Hulliger and Mooser (1965) and Goodenough (1972). The assignment of d-orbitals to the various energy states is based on electrostatic considerations in a coordinate system with the z-axis along the short Fe-S interaction in marcasite (see Figure 10).

## Part 2. Experimental and theoretical methods

### 2.1 Synthesis.

Marcasite and pyrite single crystals were obtained from an autoclave synthesis similar to the one outlined by Drábek *et al.* (2005).[65] A glass vial was cut to fit inside a teflon-coated steel autoclave and filled with 3 mL saturated iron sulphate ($FeSO_4 \cdot 7H_2O$) solution. 4 mL thiosulfate ($Na_2S_2O_3 \cdot 5H_2O$) solution (~1 M) was added to the autoclave and the glass vial with the iron sulphate solution was placed inside. The autoclave was closed and heated at 200° for around 120 hours. The marcasite product was obtained in the form of thin plates on the iron sulphate solution/gas interface and on the walls of the glass vial. Very small impurity amounts of minute pyrite single crystals were found by careful investigation of the sample under a high-magnification optical microscope.

### 2.2 Data collection.

Single crystal synchrotron X-ray diffraction data were collected at the ChemMatCARS beam line, 15-ID-B, at the Advanced Photon Source, ANL, Chicago on two single crystals of $FeS_2$ with the marcasite and pyrite structure, respectively. An octahedrally shaped ~10x10x10(3) $\mu m^3$ sized pyrite crystal and a plate-like ~5x7x10(3) $\mu m^3$ sized marcasite crystal were glued onto very thin glass fibres. A Bruker APEX II CCD detector was used to record the diffracted intensities at $\lambda$ = 0.4428 Å and $T$ = 10(5) K. A total of 15 and 23 full rotation (360°) $\varphi$-scans were collected for the pyrite and marcasite crystals, respectively. The $\varphi$-scans were collected at $2\theta$ angles of 0 °, 10°, 30° and 50° and differing $\omega$-angles with exposure times of 0.3 seconds and, for a few of the high-order runs, 0.5 seconds.

### 2.3 Data reduction.

The integration was carried out with SAINT$^+$ in which the integration box sizes were optimized manually by careful inspection of each run.[66] Three of the runs from the pyrite data collection were omitted for the final data processing, due to high $R_{symm}$ values, without affecting the completeness. The data were scaled in the program SADABS[67] which was also used to carry out an absorption and oblique correction. Finally, data averaging was performed with the program SORTAV.[68, 69] Selected crystallographic data are listed in Table 2.

### 2.4 Theoretical calculations.

Theoretically derived electron densities and structure factors of the $FeS_2$ marcasite and pyrite structures were obtained from periodic *ab-initio* DFT calculations in the experimental geometry using the WIEN2k program package. Calculations were done using the PBE functional on 21×17×27 (marcasite) and 17×17×17 (pyrite) $k$ grids with $RK_{max}$=8.5. The charge density within the atomic spheres was expanded to include spherical harmonics up to $l$=10. Atom and orbital-projected DOS were calculated using the QTL subprogram, and these were furthermore used to obtain d-orbital populations using the local coordinate system shown in Figure 10.

Table 2. Crystallographic information and experimental details.

| | *Pyrite* | *Marcasite* |
|---|---|---|
| Formula | $FeS_2$ | $FeS_2$ |
| Crystal system | Cubic | Orthorhombic |
| Space group | *Pa-3* (205) | *Pnnm* (58) |
| $Z$ | 4 | 2 |
| $\mu$ (mm$^{-1}$) | 2.79 | 2.72 |
| $T$ (K) | 10(5) | 10(5) |
| $\lambda$ (Å) | 0.4428 (28 keV) | 0.4428 (28 keV) |
| Crystal size (μm) | ~10x10x10 | ~5x7x15 |
| $a$(Å) | 5.4155(2) | 4.4330(3) |
| $b$(Å) | - | 5.4261(3) |
| $c$(Å) | - | 3.3887(2) |
| $\alpha,\beta,\gamma$(°) | 90 | 90 |
| $V$ (Å$^3$) | 158.82(2) | 81.51(2) |
| $T_{min}$, $T_{max}$ | 0.89, 0.95 | 0.91, 0.96 |
| Completeness | 99.5 % | 97.2 % |
| $N_{measured}$, $N_{unique}$ | 36550, 663 | 29560, 1041 |
| $R_{int}$, <$N$> | 4.54 %, 55.1 | 4.47 %, 28.4 |
| $(\sin\theta/\lambda)_{min}$, $(\sin\theta/\lambda)_{max}$ (Å$^{-1}$) | 0.160, 1.439 | 0.146, 1.427 |

### 2.5 Multipole refinements.

A multipole model based on the Hansen-Coppens formalism[70] was refined against each of the two experimental and theoretical data sets using the program XD2006.[71] The aspherical atom models employ scattering factors derived from STO relativistic wave functions found in the VM data bank of XD2006. All the symmetry-allowed multipole parameters up to the hexadecapole level were refined for each atom for both experimental and theoretical structure factors. In the experimental data refinement the scale factor, the atomic positions, and the ADPs were allowed to vary as well. Also, in the case of marcasite, an isotropic, Type I extinction correction was fitted whereas for pyrite, the Type II extinction correction was found to perform better; in both cases a Lorentzian mosaic distribution is assumed.[72, 73] Anomalous dispersion was

included in the model and only reflections for which I/σ(I)>2 and sinθ/λ<1.43 Å$^{-1}$ (pyrite) or sinθ/λ<1.41 Å$^{-1}$ (marcasite) were used together with statistical weights (1/σ$^2$(I)). For the two theoretical data sets, a cut-off of sinθ/λ<1.43 Å$^{-1}$ and unit-weights were applied.

Concerning the modelling of the valence electrons on Fe as well as the radial description of S, refinement of several different models has been attempted for the two $FeS_2$ structures. The Fe valence consists of a localized 3d shell and a diffuse 4s shell (Figure 3). Describing these two features simultaneously through fitting of the valence density can be difficult. In particular, refining a model describing the diffuse 4s valence electrons against experimental data is generally troublesome due to the fact that their main contribution to the scattered intensity lie in a few of the lowest-order reflections which are also the part of the data most severely affected by extinction effects.[26, 74-76] The final approach taken by Stevens *et al.* (1980) towards this problem in the case of pyrite was to transfer the two 4s electrons on Fe to the S valence, and leave only the 3d radial functions for the description of outer shell on Fe. The difference between the current study and the results of Stevens *et al.* is that inclusion of the population of the 4s shell as a variable in the refinement resulted in a physically meaningful positive population in our case, whereas Stevens *et al.* obtained unreasonable values. In order to avoid a mixing of the 3d and 4s radial functions, the valence shell on Fe is split into two separate parts, each with an associated monopole governing the population that is refined. One part is related to the 3d shell, for which only even-order multipoles can be refined (due to symmetry restrictions), and the other corresponds to the 4s shell. Radial expansion contraction parameters, $\kappa$ and $\kappa'$, were refined for the Fe 3d shell, however, for the diffuse 4s part of the Fe valence only the monopole population parameter was allowed to vary (i.e. $\kappa = \kappa' = 1$). Concerning the description of the sulphur valence shell, a combination of 3s and 3p type radial functions ($3s^2 3p^4$) were employed and a single valence population parameter was refined. The set of optimized $n_l$ radial function parameters for S determined by Dominiak *et al.* (2006) were used, which means that the standard set $n_l$=(4,4,4,4) was substituted by the set $n_l$=(2,4,6,8).[77, 78] The optimized radial functions are illustrated in Figure 3 from which it can be seen that the multipole function for the dipole ($l$=1) is significantly contracted whereas the higher order multipoles ($l$=2,3,4) are becoming more diffuse for $n_l$=(2,4,6,8) compared with the standard functions ($n_l$=4 for all $l$). One of the arguments for this choice of parameters (apart from lower $R$ factors and residual density, $\Delta\rho$) is that the resulting multipole-refined theoretical EDD reproduces the topology of the direct theoretical density better than when the standard $n_l$-set is used. In particular, a negative value of the Laplacian at the S-S bond critical point (see Part III) was obtained with the modified model but not with the standard model.[27] The results of the multipole refinements are presented in Table 3 and in the Supporting Information.

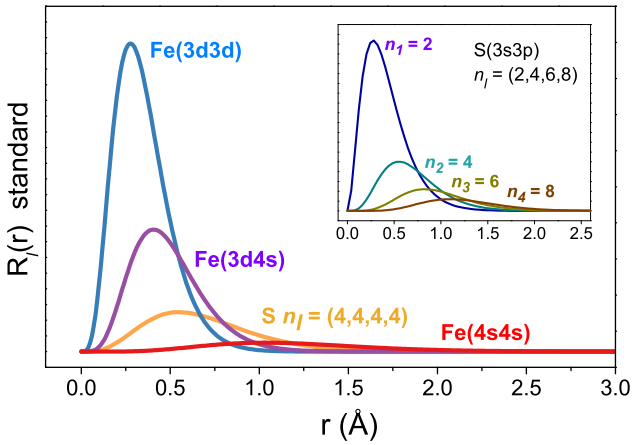


Figure 3. Standard radial valence density functions, $R_l$, plotted as function of the radial distance, r, from the atomic nuclei for various combinations of valence shells of S ($n_l$=4 for $l$=1-4) and Fe ($n_l$=4 for 3d3d, $n_l$=5 for 3d4s, $n_l$=6 for 4s4s for $l$=1-4). *Inset:* The modified radial functions of S using $n_l$=(2,4,6,8) for the multipoles with $l$=(1,2,3,4), respectively. The two plots are on arbitrary scales with respect to each other and they are both based on the Slater-type radial functions used in the Hansen-Coppens formalism. An $\alpha_l$ value of 3.8512 bohr$^{-1}$ was used for S.[78] In the case of Fe, $\alpha_l = 2 \cdot \zeta_{ave}$, where $\zeta_{ave}$ is a population-weighted average of the ζ-values associated with each valence orbital (3d, 4s) obtained from the VM databank in XD2006.[71, 77, 79]

Table 3. Results from multipole refinements against experimental and theoretical data. $s$ = sinθ/λ. $N_{refl}$ is the number of used reflections with $I/\sigma(I)>2$. For pyrite, $x$(S)=$y$(S)=$z$(S) and $U_{11}=U_{22}=U_{33}$. In both cases, ($x$,$y$,$z$)=(0,0,0) for Fe. $Q_{MM}$ are the atomic charges derived from the multipole populations. Max extinc. relates to the most extinction affected (hkl) reflection.

| | *Pyrite* | | *Marcasite* | |
|---|---|---|---|---|
| | experiment | theory | experiment | theory |
| $s_{max}$ (Å$^{-1}$) | 1.43 | 1.43 | 1.41 | 1.43 |
| R($F$) (%) | 0.73 | 0.08 | 0.82 | 0.07 |
| R($F^2$) (%) | 1.34 | 0.11 | 1.38 | 0.11 |
| $N_{refl}$ | 588 | 749 | 874 | 1192 |
| ±Δρ (e/Å$^3$) | -0.40/+0.44 | -0.16/+0.14 | -0.55/+0.57 | -0.16/+0.09 |
| ±Δρ (e/Å$^3$) $s$<0.8 Å$^{-1}$ | -0.29/+0.20 | -0.07/+0.07 | -0.31/+0.28 | -0.09/+0.07 |
| $x$ (S) | 0.384879(6) | 0.38488 | 0.20003(2) | 0.20005 |
| $y$ (S) | - | - | 0.37820(1) | 0.37819 |
| $U_{11}$ (Fe) | 0.00173(1) | - | 0.00154(2) | - |
| $U_{22}$ (Fe) | - | - | 0.00177(2) | - |
| $U_{33}$ (Fe) | - | - | 0.00180(2) | - |
| $U_{12}$ (Fe) | -0.00001(0) | - | 0.00000(1) | - |
| $U_{11}$ (S) | 0.00208(2) | - | 0.00193(3) | - |
| $U_{22}$ (S) | - | - | 0.00212(2) | - |
| $U_{33}$ (S) | - | - | 0.00214(2) | - |
| $U_{12}$ (S) | 0.00000(1) | - | -0.00014(1) | - |
| $P_{3d}$ (Fe) | 6.1(2) | 6.008(7) | 6.0(1) | 5.978(6) |
| $P_{4s}$ (Fe) | 0.4(4) | 1.74(2) | 1.5(2) | 1.84(2) |
| $P_{valence}$ (S) | 6.7(2) | 6.13(1) | 6.2(1) | 6.093(9) |
| $Q_{MM}$(Fe) | +1.5(6) | +0.25(3) | +0.6(4) | +0.19(2) |
| $Q_{MM}$(S) | -0.7(2) | -0.13(1) | -0.2(1) | -0.093(9) |
| $\kappa$(Fe) | 0.97(1) | 0.9924(4) | 0.97(1) | 0.9949(4) |
| $\kappa'$ (Fe) | 1.04(3) | 1.035(5) | 1.06(4) | 1.040(5) |
| $\kappa$(S) | 0.961(9) | 0.9848(5) | 0.985(9) | 0.9870(4) |
| $\kappa'$ (S) | 0.93(7) | 0.966(4) | 0.93(5) | 0.954(4) |
| Max extinc. | 5.6 % (200) | - | 5.6 % (101) | - |

### 2.6 Quality of refinement.

Evaluating the quality of the models fitted to the four data sets in terms of normal probability and $\Sigma F_o^2/\Sigma F_c^2$ plots (Figure S3-S4, S13), *R*-values and residual density (Table 3, Figure 4) provides highly satisfying results in all cases taking into the account the high resolution of both the experimental and theoretical data sets, and the high concentration of electron density in these inorganic, highly symmetric structures.[28] In order to take a closer look at the distribution of residual density peaks around the atoms, plots of the residual density in different planes of the unit cell have been evaluated for the multipole refinements against the experimental data (Figure 4 and Figure S6-S7). The residual density features are found to be reasonably low, though small systematic features are found around the iron atom in both structures which might indicate a need for improved radial functions for this element as well. In this context it is important to note that both Fe and S are situated at high-symmetry sites in the two structures implying a potential risk of error accumulation at or around these as well as other high-symmetry positions in the unit cell.[80, 81] In case of the theoretical data sets, similar symmetrical features around iron are vaguely seen; however, the highest residuals are found in the vicinity of the atomic cores (Figure S14-S15) and could probably be ascribed to the radial functions.[82, 83]

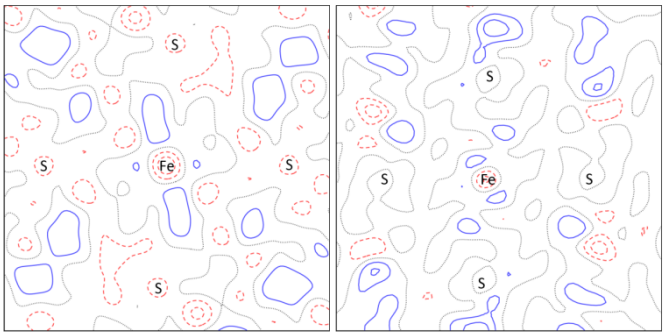


Figure 4. Residual density based on reflections with $\sin\theta/\lambda < 0.8$ Å$^{-1}$ in one of the $FeS_4$ planes of pyrite (left) and marcasite (right). The increment in the contours is 0.1 eÅ$^{-3}$. Positive contours are plotted with full, blue lines. Negative contours are plotted with dashed, red lines. The dotted, black lines are the zero contours.

In general, the results are in good agreement with respect to the Fe 3d and S valence density parameters in all four cases. The population of the iron 3d shell, $P_{3d}$, refines to a value of almost exactly 6 *e* in all four cases as expected, in contrast to the study of Stevens *et al.* which yielded a value of 4.4 *e*. Considering the population of the 4s valence shell obtained from multipole refinement against the two marcasite data sets, values of around 1.6 and 1.8 *e* are obtained from experiment and theory, respectively, indicating a good agreement between these two models as well. Also, for the refinement against the theoretical pyrite data a value in the same range (~1.7 *e*) is obtained. However, the experimental pyrite data yields a surprisingly low value of only 0.4(4) *e* and a correspondingly higher S valence population. Considering the previously mentioned problems associated with the fitting of the 4s population parameter, this is not surprising. The major scattering contribution from the 4s shell is below 0.2 Å$^{-2}$ for which there are four reflections in the marcasite data set, but only two reflections in the case of pyrite due to the higher space group symmetry. Additionally, it is a well-known fact that the atomic charges obtained from multipole refinement are ambiguous due to overlap of the rather diffuse multipole functions on neighbouring atoms.[84, 85] As shall be seen later, the discrepancy between the experimental and theoretical atomic charges for pyrite is smaller when evaluated from the atomic basin (ATB) populations.

## Part 3. 2-center chemical bonding in $FeS_2$

### 3.1. Static deformation densities

The static model deformation densities, $\rho_{def} = \rho_{model} - \rho_{IAM}$ (IAM = Independent Atom Model), around Fe and in the various $FeS_4$ planes of the two structures are shown in Figure 5 and Figure S8 for the experimental EDDs. These plots show the expected features of an unfilled 3d valence around Fe in an electrostatic pseudo-octahedral field,[26, 28] and the distorted character of the two octahedral fields is reflected in the deformations around the Fe sites which are not cubically symmetric. In accordance with the predictions of ligand field theory, exemplified in Figure 2, the deformation density of Fe shows maxima pointing towards the faces of the octahedra and minima pointing towards the six ligands. This complies with the view of localized 3d electrons being preferentially in the $t_{2g}$ orbitals. The positive density peaks in the internuclear Fe-S regions strengthen the idea of Fe $e_g$ orbitals being involved in Fe-S bond formation and indicate that some degree of covalence is present. Also, there is a hint that the axial (vertical) Fe-S interactions in marcasite are more covalent than the longer equatorial ones (Figure 5, right).

The static model deformation density in the $FeS_4$ plane of pyrite qualitatively agrees with the dynamic model deformation density plot of Stevens *et al.* (1980) with respect to the fact that, along the line joining Fe and S, negative density (charge depletion) is found in the vicinity of Fe. However, the positive peaks indicating charge accumulation around the midpoint of the Fe-S bond is absent in the plot of Stevens *et al.*. In spite of this, the authors anticipate some degree of covalence in the Fe-S interaction based on the fact that this would destabilize the S-S bond in agreement with the long S-S bond length observed in $FeS_2$ (d(S-S) = 2.16 Å) compared to the more ionic disulphide compound, $SrS_2$ (d(S-S) = 2.103 Å)[26, 86] Also, one should keep in mind that the plots cannot be directly compared since they depict different planes and since one is based on the static model density whereas the other one is dynamic and, as a consequence, more diffuse. Along these lines, Stevens *et al.* suggest that the absence of the covalent density peak in the Fe-S internuclear region can most likely be assigned to the diffuseness of the density.

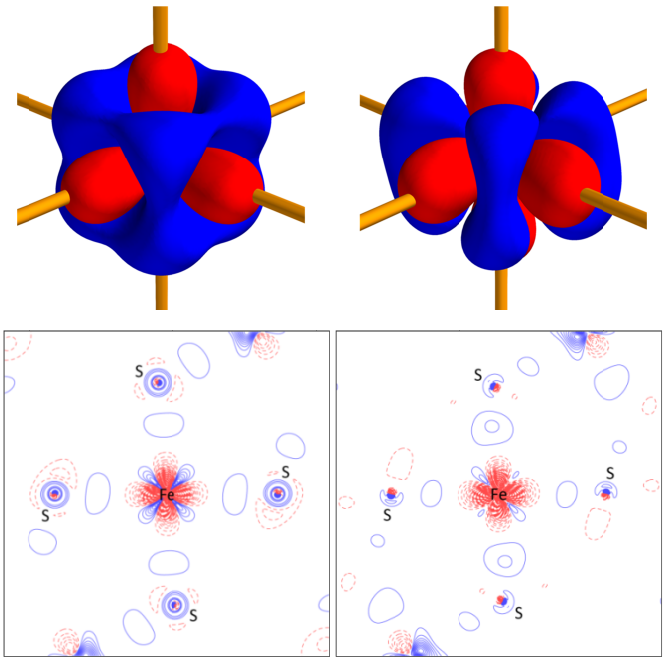


Figure 5. Top: Experimental static deformation densities around Fe for pyrite (left) and marcasite (right) plotted using isosurface values of ±0.25 eÅ$^{-3}$. Bottom: Static deformation densities for the Fe-S interactions in pyrite (left), and for the axial and equatorial Fe-S interactions in marcasite (right). The increment in the contours is 0.1 eÅ$^{-3}$. Positive contours are plotted with full, blue lines. Negative contours are plotted with dashed, red lines.

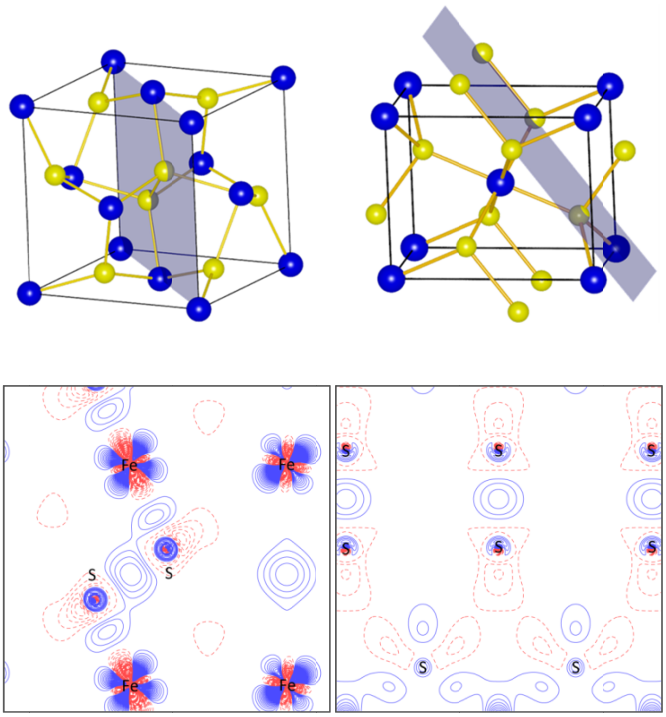


Figure 6. Contour plots of the experimental static deformation density (bottom) in a plane (top) containing the S-S dimer in pyrite (left) and marcasite (right). The contour increment is 0.05 eÅ$^{-3}$. Contours are identified as in Figure 5.

Concerning the static deformation density of the $S_2$ dumbbells (Figure 6) similar features indicative of covalent bonding are found for both structures: density is concentrated in the internuclear region and depleted in the regions opposite the S-S bond. The static deformation density in the plane of the $S_2$ dumbbells in pyrite compares well with the results of the theoretical DFT study of Zeng and Holzwarth[87] and in general there is good agreement between experiment and theory (see Figure S16-S17 in the Supporting Information). Zeng and Holzwarth attribute the negative peak in the vicinity of S to charge removal from the anti-bonding sulphur pσ* states.

### 3.2. Topological analysis

The experimental and theoretical electron densities resulting from the multipole refinements as well as the direct density distributions obtained from the WIEN2k calculations of pyrite and marcasite are analysed using the QTAIM approach developed by Bader.[32] A bond critical point (bcp), which is a requirement for the presence of a bonding interaction, is found exclusively for each of the unique nearest neighbour Fe-S and S-S bonds in the two structures with no sign of additional interactions e.g. between the Fe-Fe centres or the $S_2$ dumbbells as suggested by several authors.[12-14, 47, 56] In Table 4, the topological descriptors evaluated at the bcps (b) are shown. Comparing, qualitatively good agreement is found between experiment and theory. Such good agreement between the topology of the experimentally derived electron densities and theory bears witness of the high quality of the experimental data and of the adequacies of the multipole refinements in a fairly challenging case, despite the documented limitations of the multipole model.[27, 30, 88, 89]

In all cases the S-S interaction can be described as a covalent homoatomic bond given the lengths of atomic interaction lines (AIL) and the negative Laplacian values (Table 4). Also, the bcp is located exactly in the middle of the bond at a distance from the nuclei which is close to the covalent radius of sulphur (~1 Å).[90]

Identifying the nature of the Fe-S interactions is more difficult and cannot be done relying uniquely on the properties evaluated at the bcp. Considering the sign of the Laplacian only, the interaction would be described as a closed shell interaction.[91, 92] However, a positive $\nabla^2\rho_b$ is not surprising considering that the bcp is located in the M depletion region of iron.[46, 93-97] Furthermore, the comparisons of Laplacian profiles in Figure 7 suggest a different situation. As can be seen, a more negative $\nabla^2\rho_b$ with respect to a spherical Independent Atom Model reference density is found for all the Fe-S interactions. This indicates that there is some degree of charge accumulation between Fe and S, as indicated by the static deformation densities, even though this is not revealed by the sign of the Laplacian at the bcp.

Table 4. Results from topological analysis of experimental (experiment) and theoretical (W2k) densities for marcasite (*m*) and pyrite (*p*). MM refers to theoretical electron densities obtained from multipole refinement, and CRYST98 to the results of Gibbs *et al.*[24]. The TOPXD program[85] has been used for the multipole fitted densities. *d*: shortest distance between the atoms in Å. AIL: length of the atomic interaction line in Å. X: either Fe or S. b: bond critical point (bcp). $\rho_b$: electron density in e/Å$^3$ evaluated at the bcp. $\nabla^2\rho_b$: Laplacian of the electron density in e/Å$^5$ evaluated at the bcp.

| | | *d* | $AIL_{X-b}$ | $AIL_{S-b}$ | $\rho_b$ | $\nabla^2\rho_b$ |
|---|---|---|---|---|---|---|
| *m* Fe-S1 | experiment | 2.2355 | 1.007 | 1.233 | 0.606 | 5.512 |
| | W2k MM | 2.2355 | 1.016 | 1.220 | 0.559 | 5.662 |
| | W2k | | 1.016 | 1.220 | 0.581 | 4.803 |
| | CRYST98 | 2.231 | 1.024 | 1.207 | 0.598 | 5.140 |
| *m* Fe-S2 | experiment | 2.2530 | 1.013 | 1.241 | 0.528 | 5.981 |
| | W2k MM | 2.2530 | 1.016 | 1.237 | 0.549 | 5.437 |
| | W2k | | 1.019 | 1.235 | 0.561 | 4.711 |
| | CRYST98 | 2.250 | 1.028 | 1.222 | 0.575 | 4.967 |
| *p* Fe-S2 | experiment | 2.2631 | 1.009 | 1.255 | 0.526 | 6.205 |
| | W2k MM | 2.2631 | 1.018 | 1.246 | 0.538 | 5.542 |
| | W2k | | 1.021 | 1.242 | 0.552 | 4.666 |
| | CRYST98 | 2.263 | 1.032 | 1.231 | 0.565 | 4.923 |
| *m* S-S | experiment | 2.2119 | 1.106 | 1.106 | 0.825 | -0.370 |
| | W2k MM | 2.2120 | 1.106 | 1.106 | 0.774 | -0.358 |
| | W2k | | 1.106 | 1.106 | 0.781 | -1.406 |
| | CRYST98 | 2.212 | 1.106 | 1.106 | 0.762 | -0.124 |
| *p* S-S | experiment | 2.1597 | 1.080 | 1.080 | 0.953 | -0.902 |
| | W2k MM | 2.1596 | 1.080 | 1.080 | 0.850 | -1.045 |
| | W2k | | 1.080 | 1.080 | 0.855 | -2.226 |
| | CRYST98 | 2.178 | 1.089 | 1.089 | 0.806 | -0.614 |

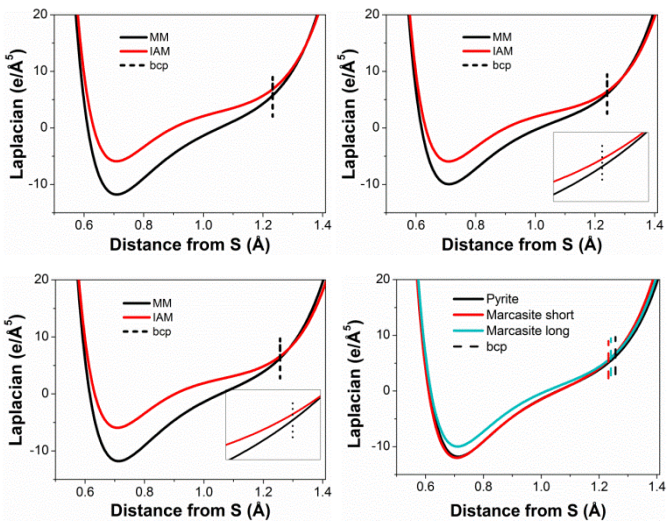


Figure 7. Laplacian profiles along the line joining the nuclei for the short (top, left) and long (top, right) S-Fe interactions in marcasite, and for the S-Fe interaction in pyrite (bottom, left). The profiles are obtained from the multipole refined (black lines) and the IAM (red lines) density based on experimental data. The insets show an enlargement of the region around the bcp. A comparison of the S-Fe bond paths for pyrite (black line) and marcasite (red and turquoise line) based on the experimental multipole densities is also shown (bottom, right).

Another hint comes from the position of the bcps. In all cases the distance of the AIL from Fe to the bcp is significantly shorter than its covalent radius (~ 1.3 Å)[90] but longer than the ionic radius (~ 0.75 Å for $Fe^{2+}$).[98] This would indicate a picture in-between the neutral and doubly ionized description of iron.

A much clearer view is obtained when analysing the local energy densities which are obtained through the adoption of the Abramov approximation.[99] In Table 5 the local kinetic, potential, and total energy density evaluated at the Fe-S and S-S bcps (b) are reported for the experimental and theoretical EDDs of pyrite and marcasite obtained from multipole refinement.

According to the classification schemes developed by Macchi, Sironi, Proserpio and Gatti,[95, 96, 100] the covalent nature of the S-S bonds is emphasized by the negative total energy density, $H_b<0$, and by $G_b/\rho_b<1$. The same description emerges from Espinosa's classification[101] ($|V_b|/G_b>2$). When the two polymorphs are compared, the values of $\rho_b$, $\nabla^2\rho_b$, $H_b$ as well as the bond lengths, suggest a slightly more covalent S-S interaction in pyrite compared to marcasite. Furthermore, the mixed shared/closed shell nature of the Fe-S interactions previously suggested is now confirmed. In all cases the total energy density, $H_b$, is negative which indicates that all the Fe-S interactions have some degree of covalent character. The values of $G_b/\rho_b$~1 are typical for donor-acceptor interactions, while a value of $|V_b|/G_b$ between 1 and 2 is associated with the so called "transit region" of incipient covalent bond formation, on the border between shared and closed shell interactions. The value of $\rho_b$ is fairly low; however, as pointed out by Macchi *et al.* and others, the fact that $\rho_b$ is small for diffuse interactions involving heavy elements is not necessarily a sign of a weak bond, but could rather be an indication of the diffuseness of the bonding electrons.[95, 100]

Comparing the topological descriptors evaluated at the bcp (Table 4 and 5) for the two polymorphs, the three different Fe-S interactions are clearly very similar. However, as evidenced by the shorter bond distance, the slightly higher $\rho_b$, the slightly smaller $\nabla^2\rho_b$ and the slightly more negative $H_b$, the shorter Fe-S interaction in marcasite appears to be somewhat more covalent than the others. This is consistent with the less covalent S-S bond with respect to pyrite, as previously discussed, and the smaller charge found on the iron atom (see Part IV). In summary, the corresponding nature of the Fe-S and S-S interactions in the two structure types are in good agreement with the proposition that a strengthening of the Fe-S interaction will cause a destabilization of the S-S bond as mentioned in the introduction.[16, 26] This may be related to the speculations of Eyert *et al.* who, based on electronic structure DFT calculations on pyrite, conclude that the chemical stability of the compound can be attributed mainly to Fe-S bonding.[6] Assuming that the same arguments hold for the marcasite compound, one would expect this to be the more stable polymorph which is not the case.[63] In this context one must keep in mind, though, that the degree of covalency cannot generally be equated with the overall bond strength since the electrostatic contribution to the bond energy cannot be ignored.

Table 5. Local kinetic, G, potential, V, and total, H energy densities at the bond critical points (b). The values are estimated from the experimental (exp) and theoretical (theory) densities obtained from multipole refinements using the functional approximation of Abramov.[99] All values are in atomic units.

| | | | $G_b$ | $G_b/\rho_b$ | $V_b$ | $H_b$ | $\lvert V_b\rvert/G_b$ |
|---|---|---|---|---|---|---|---|
| Fe-S1 | *m* | exp | 0.606 | 1.00 | -0.826 | -0.220 | 1.36 |
| | | theory | 0.569 | 1.02 | -0.742 | -0.173 | 1.30 |
| Fe-S2 | *m* | exp | 0.556 | 1.05 | -0.694 | -0.138 | 1.25 |
| | | theory | 0.550 | 1.00 | -0.719 | -0.169 | 1.31 |
| | *p* | exp | 0.565 | 1.07 | -0.696 | -0.131 | 1.23 |
| | | theory | 0.545 | 1.01 | -0.702 | -0.157 | 1.29 |
| S-S | *m* | exp | 0.566 | 0.69 | -1.158 | -0.592 | 2.05 |
| | | theory | 0.508 | 0.66 | -1.041 | -0.533 | 2.05 |
| | *p* | exp | 0.700 | 0.73 | -1.463 | -0.763 | 2.09 |
| | | theory | 0.564 | 0.66 | -1.202 | -0.638 | 2.13 |

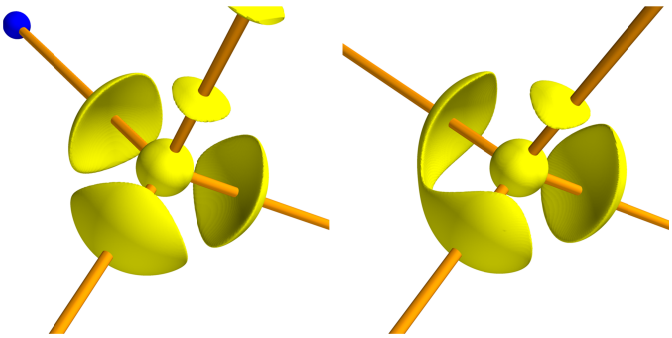

Figure 8: Three-dimensional isosurface plot of the experimental Laplacian for the sulphur atom in pyrite (left) and marcasite (right) at isosurface values of -8 e/Å$^5$ (left) and -7 e/Å$^5$ (right). The S-S bond points towards the top right corner and the short Fe-S interaction in marcasite points towards the lower right corner

## Part IV. Atomic charges and density distributions

### 4.1 Density near sulphur.

Despite the ambiguities of the Laplacian, it is possible to draw some quantitative conclusions directly from the Laplacian topology. Laplacian isosurfaces for sulphur and iron are shown in Figure 8 and Figure 9, respectively, and the positions of the maxima in $-\nabla^2\rho$ found within the valence shell charge concentration, or VSCC, for each atom have been located (see Figure S11-12, S18-23 and Table S4 in the Supporting Information). The pseudo-tetrahedral coordination of sulphur resulting from sp$^3$ hybridization of the electronic valence states is emphasized by four maxima in the sulphur VSCC which point towards the bonded neighbours. In the case of marcasite, there is a distinction between the two maxima associated with the longer Fe-S bonds ($\rho_{max}$=1.236 eÅ$^{-3}$, $-\nabla^2\rho_{max}$=9.96 eÅ$^{-5}$) and the one maxima pointing in the direction of the short Fe-S interaction ($\rho_{max}$=1.325 eÅ$^{-3}$, $-\nabla^2\rho_{max}$=12.05 eÅ$^{-5}$). An elaborate rationalization of the sulphur VSCC maxima with respect to minimization of charge repulsion and the geometry of the marcasite structure has been given elsewhere by Cenedese *et al.*[46] Accordingly we find, both from experiment and theory, that sulphur VSCC maxima along the equatorial Fe-S bonds are displaced from the interatomic line in the direction away from the smaller S-Fe-S angle (α~82°, see Figure 2) so as to minimize repulsion between the charge accumulation regions on the sulphur atoms (Figure S22). For comparison, the sulphur VSCC maxima associated with the Fe-S bond in pyrite lie closer to the Fe-S interatomic line. This is in accordance with the fact that the smallest S-Fe-S angle (~86°) in pyrite is larger than the α-angle in marcasite (see Table 1). However, though the displacement away from the Fe-S interatomic line is small in pyrite, there is still a tendency for the sulphur VSCC maxima to be slightly shifted towards the regions of space associated with the large S-Fe-S angle in order to minimize charge repulsion, and this displacement is slightly more pronounced for experiment than theory (Figure S11 and S18).

Table 6. Atomic basin integrations of Fe and S in marcasite (*m*) and pyrite (*p*) based on the experimental (experiment) and theoretical (W2k) densities. MM refers to theoretical electron densities obtained from multipole refinement, and CRYST98 to the results of Gibbs *et al.*[24] All values are reported in atomic units. $N$ is the atomic electron population, $Q_{QTAIM}$ is the atomic charge, $V$ is the total atomic basin volume, and $\mu$ is the magnitude of the atomic dipole moment. $L$ is the Lagrangian, $L_\Omega=-\frac{1}{4}\int_\Omega\nabla^2\rho d\tau$, which is a measure of the accuracy of the numerical integration of the atomic basin Ω.[71]

| | | $N$ | $Q_{QTAIM}$ | $V$ | $L$ | $\mu$ |
|---|---|---|---|---|---|---|
| Fe *m* | experiment | 25.37 | 0.633 | 67.19 | $7.1\cdot10^{-3}$ | 0.012 |
| | W2k MM | 25.44 | 0.562 | 67.59 | $2.5\cdot10^{-3}$ | 0.008 |
| | W2k | - | 0.688 | - | - | - |
| | CRYST98 | - | 0.67 | - | - | - |
| Fe *p* | experiment | 25.08 | 0.919 | 61.31 | $1.6\cdot10^{-3}$ | 0.005 |
| | W2k MM | 25.40 | 0.596 | 67.24 | $1.2\cdot10^{-3}$ | 0.012 |
| | W2k | - | 0.673 | - | - | - |
| | CRYST98 | - | 0.67 | - | - | - |
| S *m* | experiment | 16.31 | -0.305 | 103.36 | $2.9\cdot10^{-3}$ | 0.070 |
| | W2k MM | 16.27 | -0.274 | 103.52 | $2.4\cdot10^{-3}$ | 0.167 |
| | W2k | - | -0.3428 | - | - | - |
| | CRYST98 | - | -0.34 | - | - | - |
| S *p* | experiment | 16.46 | -0.457 | 103.27 | $8.0\cdot10^{-4}$ | 0.051 |
| | W2k MM | 16.29 | -0.293 | 100.33 | $1.7\cdot10^{-3}$ | 0.237 |
| | W2k | - | -0.3380 | - | - | - |
| | CRYST98 | - | -0.34 | - | - | - |

### 4.2 Atomic charges.

Dividing the valence density into atom-centred multipolar contributions is a necessary approximation that allows us to easily fit a reasonably simple model to the data; however, the multipole populations do not offer a clear-cut definition of atomic charge since, as mentioned previously, there might be a substantial overlap of the multipole functions on neighbouring atoms.[84, 85] This holds in particular for the Fe(4s) valence shell since this is very diffuse and extends far out in space, and it also applies to the fairly diffuse S valence[18] (see Figure 3). However, in spite of the ambiguities related to the multipole charges, comparison with the QTAIM derived atomic basin (ATB) charges in Table 6 shows that fairly good agreement is found. Neglecting the results from the experimental pyrite data, the multipole populations (Table 3) estimate a charge transfer

of 0.2-0.4 *e* from Fe to the sulphur dumbbell. Similarly, the ATB integration yields values corresponding to a charge transfer from Fe in the range of 0.6-0.7 *e*. That is, both the multipole and the ATB charges are far from the formal charges expected from simple electrostatic crystal-field theory. This is not surprising considering the fairly small difference in the electronegativities of iron and sulphur, and when taking the previous results of the bonding analysis into account: The polar covalent character of the Fe-S interaction means that the electron density in the bonding region is displaced from Fe towards the surrounding sulphur atoms, but without being fully transferred, and the atomic multipole and ATB charges fully support this picture.

### 4.3 d-orbital picture and density of states.

Given that the multipolar density functions are simply mathematical constructions derived from orbital-like functions, there is no assurance that their populations can be directly related to populations of isolated-atom orbital density functions; especially not in cases where the electrons participate in bonding. However, in the special case of d-orbital density, a simple relation exists between the even-order ($l$=0,2,4) multipolar functions and the orbital density functions.[102] Furthermore, contrary to the more diffuse valence shells mentioned above, the population of the 3d shell, $P_{3d}$, is more likely to resemble the true picture since the 3d electrons are much more localized in space (Figure 3), and the assumption that these orbitals do not participate in bonding is often a good approximation for transition metal elements as the metal-ligand overlap density tends to be small. This means that 'd-orbital-like' populations can often be derived for transition metals from a multipole refinement with reasonable outcomes.[79, 103, 104]

Stevens *et al.* derived the d-orbital populations of iron in their study on pyrite $FeS_2$; however, their choice of local coordinate system on Fe for the evaluation does not lead to a straightforward interpretation of the population of the individual d states.[26, 79] In the present study, the local coordinate system of Fe has been obtained by searching on a grid for specific rotations yielding specific configurations of the d-orbital populations. This was achieved using the program WinERD.[104] The chosen orientation of the coordinate system was the one that was judged to give a meaningful chemical interpretation of the d-orbital populations for the two $FeS_2$ compounds. The 'chemical' coordinate system has the *z*-axis pointing roughly along the short Fe-S interaction while *x* and *y* point approximately in the direction of the long Fe-S bonds in marcasite (Figure 9). Analogously, all axes point, as far as possible, along the Fe-S directions in pyrite yielding the d-orbital populations given in Table 7.† The values in square brackets are obtained from the direct theoretical EDD in WIEN2k derived from the DOS in Figure 11.

The total population of the 3d shell is around six in all cases. This agrees with the widespread conventional picture found in the literature that the semiconducting, diamagnetic properties can be explained in terms of a $t_{2g}^6e_g^0$ electronic configuration on Fe.[10, 19, 105] However, inspection of the distribution of electrons among the individual d-orbitals reveals that this description is much too simplified since all d-levels are partly populated, including the $e_g$ states.

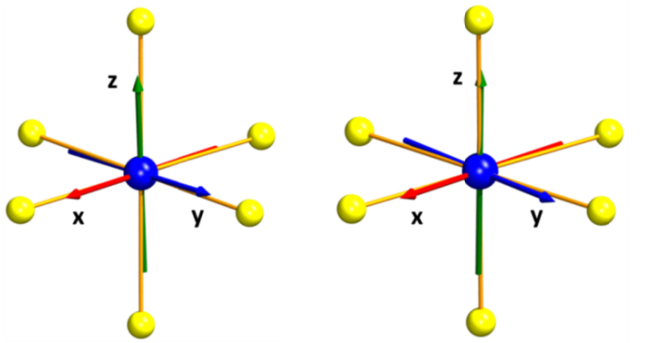


Figure 9. Local coordinate system for experimental d-orbital evaluation of pyrite (left) and marcasite (right). For marcasite, the short Fe-S interaction is pointing vertically along the z axis (green arrow).

Table 7. Fe d-orbital populations (in %) for pyrite and marcasite. The populations are evaluated from the multipole populations with respect to the coordinate system obtained from WinERD for which the axes are, as far as possible, oriented along the Fe-S interactions of Fe in the two structures.† The values in square brackets are obtained from the direct theoretical electron density in WIEN2k using the same local coordinate systems as those that are used for the multipole fitted theoretical density (Figure S24).††

| | Pyrite | | Marcasite | |
|---|---|---|---|---|
| | experiment | theory | experiment | theory |
| $d_{xy}$ | 26.7 | 25.9 [24.5] | 30.7 | 28.4 [26.3] |
| $d_{xz}$ | 25.7 | 25.0 [24.5] | 24.3 | 23.8 [23.5] |
| $d_{yz}$ | 25.7 | 25.0 [24.5] | 24.2 | 23.8 [23.5] |
| $d_z^2$ | 11.5 | 12.5 [13.3] | 12.8 | 13.7 [14.2] |
| $d_{x^2-y^2}$ | 10.5 | 11.6 [13.3] | 8.1 | 10.3 [12.4] |
| $P_{total}$ (*e*) | 6.1(2) | 6.01(1) [6.21] | 6.0(1) | 5.98(1) [6.21] |

According to the population outlined in Table 7, the same qualitative picture is obtained from both experiment and theory for both structures: $P(d_{xy})>P(d_{xz})\sim P(d_{yz})>P(d_{z2})\geq P(d_{x2-y2})$. A good agreement is also found with the Mulliken populations evaluated for marcasite $FeS_2$ in the study of Cenedese *et al.*[46]

In contrast to the local density-based approach of QTAIM analysis and the atomic orbital-based approach of the multipole model, the DOS derived from the band structure offer a non-local and energy-based description of the electronic states in solids. Generally, localized density features from non-bonding orbitals give rise to narrow bands whereas highly overlapping (covalently bonded) orbitals give rise to broad bands extending across a range of energies.[19, 106] In Figure 11 the individual contributions of the Fe d-orbital states to the total DOS obtained from *ab initio* DFT calculations are shown for pyrite and marcasite $FeS_2$. In both cases, the main contribution in the valence band near the Fermi level is given by Fe $t_{2g}$ orbitals, with negligible contributions from the S atoms. The spatially

localized nature of the $t_{2g}$ shell is corroborated by the rather limited spread in the energy states associated with these electrons. That is, the $t_{2g}$ orbitals behave mostly as non-bonding orbitals in agreement with the molecular orbital schemes proposed in literature (Figure S2), and a population greater than 1.5 *e* is always found. On the contrary, the Fe $e_g$ orbitals are located above and below the Fermi level and clearly mix with the sulphur valence states to form broad bonding and anti-bonding bands, also in accordance with the MO/band theory description presented in Part I.[6] Furthermore, the small (< 1 *e*) but non-negligible population of each of the $e_g$ orbitals indicates that the bonding part of the Fe($e_g$)-S(3s,3p) band is populated and that the charge is, to some extent, shared between Fe and S. The higher contribution of (empty) $e_g$ states above the Fermi level agrees with the statement by Kjekshus[16] and Goodenough[19] that these states are mainly anti-bonding with respect to the Fe-S interaction. In this way the d-orbital populations and DOS account for the partial covalent character of the Fe-S interactions and the diamagnetic properties of $FeS_2$. They also reflect the differences between the two polymorphs: In marcasite, the $d_{xy}$ population is higher than the population of the $d_{xz}$ and $d_{yz}$ orbitals. According to the general picture given by Goodenough on $MX_2$ marcasite compounds the $d_{xy}$ orbital on the transition metal is capable of mixing with the anion valence states whereas the $d_{xz}$ and $d_{yz}$ are non-bonding.[19] Since $d_{xy}$ is anti-bonding with respect to the anions it will be higher in energy than the other $t_{2g}$ states. When the $d_{xy}$ orbital is populated, as it inevitably is in $FeS_2$, the concomitant repulsion with the ligands in the equatorial *xy*-plane will cause a lengthening of the equatorial metal-ligand bonds in order to diminish the $d_{xy}$-anion overlap. As a result, $d_{xy}$ becomes non-bonding and is lowered in energy. This is the reason for the relative 'elongation' of the Fe-S bonds in marcasite along the *c*-axis. In pyrite, where all Fe-S interactions are equivalent and longer than those in marcasite, the $t_{2g}$-type orbitals are close to degenerate in the chosen local coordinate system and, accordingly, have almost equivalent populations and orbital-projected DOS (Table 7 and Figure 11 top).

According to the simplified but widespread electrostatic scheme depicted in Figure 2, the higher population of $d_{xy}$ in marcasite could suggest that the equatorial Fe-S bonds in marcasite are so long that the energy of $d_{xy}$ is in fact below that of $d_{xz}$ and $d_{yz}$. However, as clearly illustrated by the DOS, this local orbital-based picture is no longer valid in the extended solid where orbitals are replaced by bands. From the marcasite DOS it seems that the $d_{xy}$ states right below the Fermi level peak at higher energies than the $d_{xz}$ and $d_{yz}$, and the initial response would be to expect a higher population of the latter. The fact that this is not the case shows that there is a larger number of available $d_{xy}$ states below the Fermi level than above compared with $d_{xz}$ and $d_{yz}$ (Table 7 and Figure 11 bottom). That is, $d_{xz}$ and $d_{yz}$ contribute with a comparably higher number of states in the conduction band which, from the semiconducting, diamagnetic properties of the compound, is known to be empty. Generally, the distribution of the $t_{2g}$-states both below and above the band gap explains why the valence band can be filled despite the fact that none of the $t_{2g}$-like orbitals have populations as high as 2 *e*, as would otherwise be expected if the non-bonding d-orbitals were filled and fully localized below the Fermi energy.

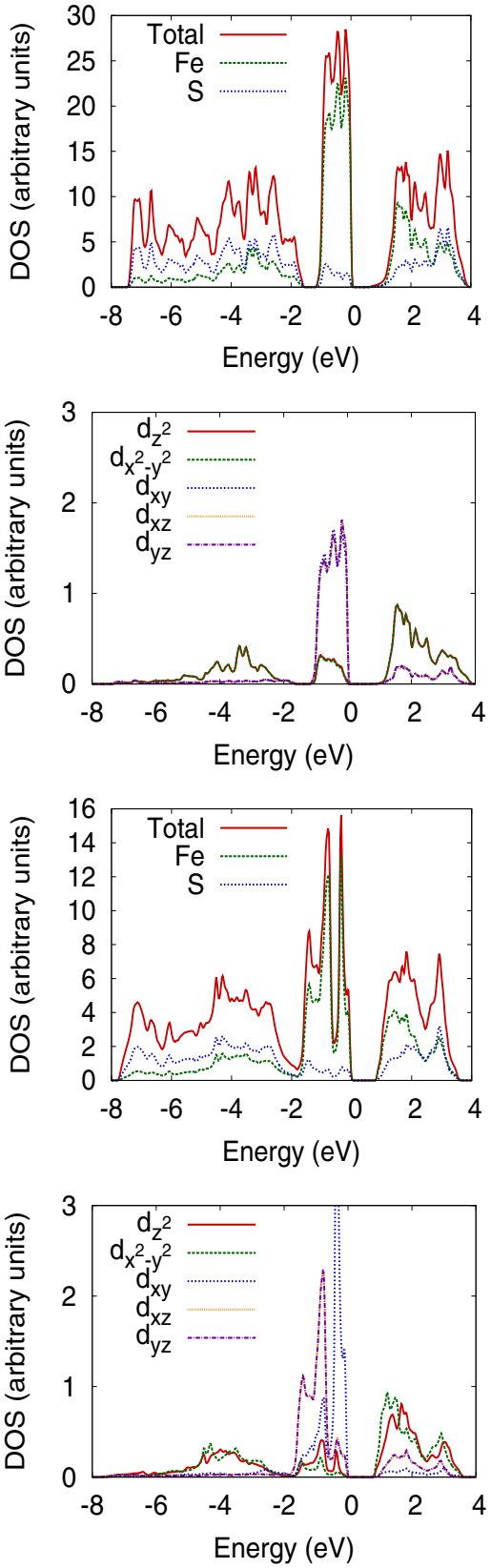

Figure 11. Total and atom-projected DOS and Individual Atomic Orbitals projected DOS of the Fe d orbital states for pyrite (top pair) and marcasite (bottom pair). The results have been obtained from the periodic DFT calculations in WIEN2k using the experimental $FeS_2$ geometries (see section 2.4).

## Conclusion

As already expected from speculations on compounds with the pyrite and marcasite structure back in the 1960's and 70', there is a close relationship between the geometry, the bonding interactions, the d-orbital populations, and the band structure of this family of materials which has now been verified from experimental electron density analysis. This has been achieved even though inorganic extended solids such as transition metal sulphides represent a great challenge for X-ray charge density determination. By utilizing high-energy synchrotron radiation, minute single-crystals, and low temperatures we have managed to collect high resolution X-ray diffraction data with limited extinction effects on two polymorphs of $FeS_2$ of sufficiently high quality to obtain an excellent match with *ab inito* periodic DFT calculations.

Analysis of the experimental and theoretical electron density distributions revealed that the Fe-S bonds are on the border between shared and closed shell interactions with both ionic and a non-negligible degree of covalent character. The charges on Fe and S of around +⅔ and –⅓ *e*, respectively, are significantly smaller than the formal +2 and −1 charges supporting the polar covalent nature of the Fe-S interactions. This description is directly obtained on a 'local' atomic level from both multipole refinements and from topological analysis. It is furthermore corroborated by band structure calculations, offering a non-local picture of the population of the electronic states in extended crystal structures, which show clear signs of covalent mixing between the valence states on sulphur and the 3d $e_g$-like states on iron. That is, irrespective of the approach taken, the same overall bonding description is obtained for the two $FeS_2$ compounds.

The major discrepancy between the two structures in terms of bonding is found to be more covalent S-S interactions and correspondingly weaker Fe-S bonds in pyrite compared to marcasite. Furthermore, the distribution of the d-orbital-like density directly reflects a difference between the two polymorphs considering that the population of the $d_{xy}$ orbital is noticeably higher than the population of $d_{xz}$ and $d_{yz}$ in marcasite, whereas the distribution of electrons among the $t_{2g}$ states in pyrite is more even. A non-negligible population of the $e_g$-like states again indicates the covalent component to the Fe-S bonding, and the diamagnetic properties of the compounds, despite the non-zero $e_g$ population, can be explained in terms of 'delocalization' of the $e_g$ electrons through hybridization with the valence states on sulphur causing them to participate in the collective electronic states extending across the entire solid.

## Acknowledgements

This work was supported by the Danish National Research Foundation (DNRF93), and the Danish Research Council for Nature and Universe (Danscatt). ChemMatCARS Sector 15 is principally supported by the National Science Foundation/Department of Energy under Grant NSF/CHE-0822838. Use of the Advanced Photon Source was supported by the U.S. Department of Energy, Office of Science, Office of Basic Energy Sciences, under Contract No. DE-AC02-06CH11357.

## Notes and references

[a] Center for Materials Crystallography, Department of Chemistry and iNANO, Aarhus University Langelandsgade 140, DK-8000 Aarhus C. Denmark..

[b] University of Toledo, Toledo, Ohio 43606, United States.

[c] ChemMatCARS, University of Chicago, Advanced Photon Source, Argonne, Illinois 60439, United States.

[d] Istituto di Scienze e Technologie Molecolari del CNR (CNR-ISTM) and Dipartimento de Chimica, Università di Milano, via Golgi 19, I-20133, Milano, Italy.

† In the case of pyrite, this is achieved when selecting the option yielding the lowest population of both $d_{z2}$ and $d_{x2-y2}$. The *x*- and *y*-axis are lying almost in one of the $FeS_4$ planes and almost along the Fe-S interactions, whereas the *z*-axis is slightly more misaligned. In the case of marcasite, the only option yielding a coordinate system for which the *z*-axis is pointing almost exactly along the shorter Fe-S bond is the one corresponding to the smallest population of $d_{x2-y2}$. The *x*- and *y*-axes are lying almost in one of the $FeS_4$ planes and almost along the Fe-S interactions, whereas the *z* axis is slightly more misaligned. The reason why the axes are not exactly along the bonds is probably related to the discretized grid used for the search.

†† The populations and DOS have also been evaluated for a local coordinate system for which the *z* axis points exactly along the short Fe-S bond in marcasite and one of the Fe-S bonds in pyrite while *x* and *y* are as close as possible and equidistant from the equatorial Fe-S bonds in marcasite and from two other Fe-S bonds in pyrite (see Table S5 and Figure S25 in the Supporting Information). No significant differences are found between the results obtained from using the two slightly different coordinate systems.

Electronic Supplementary Information (ESI) available: Additional illustrations, and figures and tables with the results from the multipole refinements and the topological analysis, together with additional results from DOS calculations. See DOI: 10.1039/b000000x/

1. W. L. Bragg, *P R Soc Lond a-Conta*, 1914, **89**, 468-489.
2. W. A. Hendrickson, *Acta Crystallogr A*, 2013, **69**, 51-59.
3. R. S. Sun, M. K. Y. Chan and G. Ceder, *Phys Rev B*, 2011, **83**, 235311.
4. A. Ennaoui, S. Fiechter, C. Pettenkofer, N. Alonsovante, K. Buker, M. Bronold, C. Hopfner and H. Tributsch, *Sol Energ Mat Sol C*, 1993, **29**, 289-370.
5. H. Tributsch, S. Fiechter, D. Jokisch, J. Rojas-Chapana and K. Ellmer, *Origins Life Evol B*, 2003, **33**, 129-162.
6. V. Eyert, K. H. Hock, S. Fiechter and H. Tributsch, *Phys Rev B*, 1998, **57**, 6350-6359.
7. C. Wadia, Y. Wu, S. Gul, S. K. Volkman, J. H. Guo and A. P. Alivisatos, *Chem Mater*, 2009, **21**, 2568-2570.



 

8. Y. C. Wang, D. Y. Wang, Y. T. Jiang, H. A. Chen, C. C. Chen, K. C. Ho, H. L. Chou and C. W. Chen, *Angewandte Chemie-International Edition*, 2013, **52**, 6694-6698.
9. J. Puthussery, S. Seefeld, N. Berry, M. Gibbs and M. Law, *J Am Chem Soc*, 2011, **133**, 716-719.
10. F. Hulliger and E. Mooser, *J Phys Chem Solids*, 1965, **26**, 429-433.
11. E. H. Nickel, *Chem Geol*, 1970, **5**, 233-241.
12. E. H. Nickel, *The Canadian Mineralogist*, 1968, **9**, 311-321.
13. G. Brostigen and A. Kjekshus, *Acta Chem Scand*, 1970, **24**, 2993-3012.
14. G. Brostigen and A. Kjekshus, *Acta Chem Scand*, 1970, **24**, 2983-2992.
15. G. Brostigen and A. Kjekshus, *Acta Chem Scand*, 1969, **23**, 2186-2188.
16. A. Kjekshus and D. G. Nicholson, *Acta Chem Scand*, 1971, **25**, 866-876.
17. J. A. Tossell, D. J. Vaughan and J. K. Burdett, *Phys Chem Miner*, 1981, **7**, 177-184.
18. D. J. Vaughan and J. R. Craig, *Mineral chemistry of metal sulfides*, Cambridge University Press, Cambridge Eng. ; New York, 1978.
19. J. B. Goodenough, *J Solid State Chem*, 1972, **5**, 144-152.
20. G. Brostigen and A. Kjekshus, *Acta Chem Scand*, 1970, **24**, 1925-1940.
21. G. Brostigen and A. Kjekshus, *Acta Chem Scand*, 1970, **24**, 1925-1940.
22. B. Hyde and M. OKeeffe, *Aust J Chem*, 1996, **49**, 867-872.
23. N. E. Brese and H. G. Von Schnering, *Z Anorg Allg Chem*, 1994, **620**, 393-404.
24. G. V. Gibbs, D. F. Cox, K. M. Rosso, N. L. Ross, R. T. Downs and M. A. Spackman, *J Phys Chem B*, 2007, **111**, 1923-1931.
25. G. V. Gibbs, R. T. Downs, D. F. Cox, N. L. Ross, C. T. Prewitt, K. M. Rosso, T. Lippmann and A. Kirfel, *Z Kristallogr*, 2008, **223**, 1-40.
26. E. D. Stevens, M. L. Delucia and P. Coppens, *Inorg Chem*, 1980, **19**, 813-820.
27. M. S. Schmøkel, J. Overgaard and B. B. Iversen, *Z Anorg Allg Chem*, 2013, **639**, 1922-1932.
28. P. Coppens, *X-ray charge densities and chemical bonding*, International Union of Crystallography; Oxford University Press, Chester, England, Oxford; New York, 1997.
29. M. S. Schmøkel, S. Cenedese, J. Overgaard, M. R. V. Jorgensen, Y. S. Chen, C. Gatti, D. Stalke and B. B. Iversen, *Inorg Chem*, 2012, **51**, 8607-8616.
30. M. S. Schmøkel, L. Bjerg, J. Overgaard, F. K. Larsen, G. K. H. Madsen, K. Sugimoto, M. Takata and B. B. Iversen, *Angewandte Chemie-International Edition*, 2013, **52**, 1503-1506.
31. M. S. Schmokel, L. Bjerg, F. K. Larsen, J. Overgaard, S. Cenedese, M. Christensen, G. K. H. Madsen, C. Gatti, E. Nishibori, K. Sugimoto, M. Takata and B. B. Iversen, *Acta Crystallogr A*, 2013, **69**, 570-582.
32. R. F. W. Bader, *Atoms in molecules : a quantum theory*, Clarendon Press, Oxford ; New York, 1990.
33. M. Birkholz, *J Phys-Condens Mat*, 1992, **4**, 6227-6240.
34. G. U. Kulkarni, P. Kumaradhas and C. N. R. Rao, *Chem Mater*, 1998, **10**, 3498-3505.
35. R. S. Gopalan, G. U. Kulkarni and C. N. R. Rao, *Chemphyschem*, 2000, **1**, 127-135.
36. J. Overgaard and D. E. Hibbs, *Acta Cryst A*, 2004, **60**, 480-487.
37. P. Munshi and T. N. G. Row, *Cryst Growth Des*, 2006, **6**, 708-718.
38. M. Schmidtmann, L. J. Farrugia, D. S. Middlemiss, M. J. Gutmann, G. J. McIntyre and C. C. Wilson, *J Phys Chem A*, 2009, **113**, 13985-13997.
39. A. A. Hoser, L. Dobrzycki, M. J. Gutmann and K. Wozniak, *Cryst Growth Des*, 2010, **10**, 5092-5104.
40. P. Munshi, C. Jelsch, V. R. Hathwar and T. N. G. Row, *Cryst Growth Des*, 2010, **10**, 1516-1526.
41. M. Gryl, A. Krawczuk-Pantula and K. Stadnicka, *Acta Cryst B*, 2011, **67**, 144-154.
42. A. A. Hoser, K. N. Jarzembska, L. Dobrzycki, M. J. Gutmann and K. Wozniak, *Cryst Growth Des*, 2012, **12**, 3526-3539.
43. A. E. Whitten, B. Dittrich, M. A. Spackman, P. Turner and T. C. Brown, *Dalton Trans.*, 2004, 23-29.
44. M. L. Huggins, *Phys Rev*, 1922, **19**, 369-373.
45. G. S. Pawley and R. P. Rinaldi, *Acta Cryst B*, 1972, **28**, 3605-3609.
46. S. G. Cenedese, C.; Schmøkel, M. S.; Iversen, B. B., unpublished work.
47. W. B. Pearson, *Z Kristallogr*, 1965, **121**, 449-462.
48. J. H. Van Vleck, *Phys Rev*, 1932, **41**, 208-215.
49. G. Brostigen and A. Kjekshus, *Acta Chem Scand*, 1970, **24**, 2993-3012.
50. T. A. Bither, R. J. Bouchard, W. H. Cloud, P. C. Donohue and W. J. Siemons, *Inorg Chem*, 1968, **7**, 2208-2220.
51. R. G. Burns, *Mineralogical applications of crystal field theory*, Cambridge U.P., London,, 1970.
52. L. Pauling and M. L. Huggins, *Z Kristallogr*, 1934, **87**, 205-238.
53. E. K. Li, K. H. Johnson, D. E. Eastman and J. L. Freeouf, *Phys Rev Lett*, 1974, **32**, 470-472.
54. J. A. Tossell, *J Chem Phys*, 1977, **66**, 5712-5719.
55. D. W. Bullett, *J Phys C Solid State*, 1982, **15**, 6163-6174.
56. P. Raybaud, J. Hafner, G. Kresse and H. Toulhoat, *J Phys-Condens Mat*, 1997, **9**, 11107-11140.
57. I. Opahle, K. Koepernik and H. Eschrig, *Comp Mater Sci*, 2000, **17**, 206-210.
58. M. Bronold, Y. Tomm and W. Jaegermann, *Surf Sci*, 1994, **314**, L931-L936.
59. C. I. Pearce, R. A. D. Pattrick and D. J. Vaughan, *Rev Mineral Geochem*, 2006, **61**, 127-180.
60. M. J. Buerger, *Am Mineral*, 1934, **19**, 37-61.
61. M. E. Fleet, *The Canadian Mineralogist*, 1970, **10**, 225-231.
62. P. Raybaud, G. Kresse, J. Hafner and H. Toulhoat, *J Phys-Condens Mat*, 1997, **9**, 11085-11106.
63. F. Gronvold and E. F. Westrum, *J Chem Thermodyn*, 1976, **8**, 1039-1048.
64. A. R. Lennie and D. J. Vaughan, *Am Mineral*, 1992, **77**, 1166-1171.
65. M. Drabek and M. Rieder, *Mineral Deposit Research: Meeting the Global Challenge, Vols 1 and 2*, 2005, 111-113.
66. Bruker, Bruker AXS Inc., Madison, Wisconsin, USA, 2007.
67. Bruker, Bruker AXS Inc., Madison, Wisconsin, USA, 2001.
68. R. H. Blessing, *J Appl Crystallogr*, 1997, **30**, 421-426.

69. R. H. Blessing and D. A. Langs, *J Appl Crystallogr*, 1987, **20**, 427-428.
70. N. K. Hansen and P. Coppens, *Acta Crystallogr A*, 1978, **34**, 909-921.
71. A. M. Volkov, P.; Farrugia, L. J.; Gatti, C.; Mallinson, P.; Richter, T.; Koritsanszky, T., 2006.
72. P. J. Becker and P. Coppens, *Acta Crystallogr A*, 1974, **A 30**, 129-147.
73. P. J. Becker and P. Coppens, *Acta Crystallogr A*, 1974, **A 30**, 148-153.
74. P. Coppens, *Coord. Chem. Rev.*, 1985, **65**, 285-307.
75. L. J. Farrugia and C. Evans, *J Phys Chem A*, 2005, **109**, 8834-8848.
76. L. J. Farrugia, C. Evans, D. Lentz and M. Roemert, *J Am Chem Soc*, 2009, **131**, 1251-1268.
77. E. Clementi and D. L. Raimondi, *J Chem Phys*, 1963, **38**, 2686-2689.
78. P. M. Dominiak and P. Coppens, *Acta Cryst A*, 2006, **62**, 224-227.
79. P. Coppens, *X-ray Charge Densities and Chemical Bonding*, International Union of Crystallography; Oxford University Press, Chester, England, Oxford; New York, 1997.
80. B. Rees, *Acta Cryst A*, 1976, **32**, 483-488.
81. D. W. J. Cruickshank and J. S. Rollett, *Acta Crystallogr*, 1953, **6**, 705-707.
82. A. Fischer, D. Tiana, W. Scherer, K. Batke, G. Eickerling, H. Svendsen, N. Bindzus and B. B. Iversen, *J Phys Chem A*, 2011, **115**, 13061-13071.
83. J. Overgaard, C. Jones, D. Dange and J. A. Patts, *Inorg Chem*, 2011, **50**, 8418-8426.
84. Y. A. Abramov, A. V. Volkov and P. Coppens, *Chem Phys Lett*, 1999, **311**, 81-86.
85. A. Volkov, C. Gatti, Y. Abramov and P. Coppens, *Acta Cryst A*, 2000, **56**, 252-258.
86. I. Kawada, K. Kato and S. Yamaoka, *Acta Cryst B*, 1976, **32**, 3110-3111.
87. Y. Zeng and N. A. W. Holzwarth, *Phys Rev B*, 1994, **50**, 8214-8220.
88. A. Volkov, Y. Abramov, P. Coppens and C. Gatti, *Acta Cryst A*, 2000, **56**, 332-339.
89. A. Volkov and P. Coppens, *Acta Cryst A*, 2001, **57**, 395-405.
90. B. Cordero, V. Gomez, A. E. Platero-Prats, M. Reves, J. Echeverria, E. Cremades, F. Barragan and S. Alvarez, *Dalton T*, 2008, 2832-2838.
91. R. F. W. Bader and H. Essen, *J Chem Phys*, 1984, **80**, 1943-1960.
92. R. F. W. Bader, P. J. Macdougall and C. D. H. Lau, *J Am Chem Soc*, 1984, **106**, 1594-1605.
93. R. P. Sagar, A. C. T. Ku, V. H. Smith and A. M. Simas, *J Chem Phys*, 1988, **88**, 4367-4374.
94. Z. Shi and R. J. Boyd, *J Chem Phys*, 1988, **88**, 4375-4377.
95. P. Macchi and A. Sironi, *Coord. Chem. Rev.*, 2003, **238**, 383-412.
96. C. Gatti, *Z Kristallogr*, 2005, **220**, 399-457.
97. G. Eickerling and M. Reiher, *J Chem Theory Comput*, 2008, **4**, 286-296.
98. R. D. Shannon and C. T. Prewitt, *Acta Crystall B-Stru*, 1969, **B 25**, 925-946.
99. Y. A. Abramov, *Acta Cryst A*, 1997, **53**, 264-272.
100. P. Macchi, D. M. Proserpio and A. Sironi, *J Am Chem Soc*, 1998, **120**, 13429-13435.
101. E. Espinosa, I. Alkorta, J. Elguero and E. Molins, *J Chem Phys*, 2002, **117**, 5529-5542.
102. E. D. Stevens and P. Coppens, *Acta Cryst A*, 1979, **35**, 536-539.
103. A. Holladay, P. Leung and P. Coppens, *Acta Crystallogr A*, 1983, **39**, 377-387.
104. J. R. Sabino and P. Coppens, *Acta Cryst A*, 2003, **59**, 127-131.
105. S. Suga, A. Kimura, T. Matsushita, A. Sekiyama, S. Imada, K. Mamiya, A. Fujimori, H. Takahashi and N. Mori, *Phys Rev B*, 1999, **60**, 5049-5054.
106. J. B. Goodenough, *J Appl Phys*, 1966, **37**, 1415-1422.



 